RESEARCH ARTICLE

ADVANCED MATERIALS
www.advmat.de

Polarity-Reversible Zero-Field Diode Effect in van der Waals Ferromagnetic Josephson Junction for Logic Operation

Guojing Hu, Yechao Han, Hui Guo, Senhao Lv, Tianqi Gao, Yunhao Wang, Zhen Zhao, Ke Zhu, Qi Qi, Guoyu Xian, Shiyu Zhu, Lihong Bao, Xiao Lin, Wu Zhou, Kun Jiang,* Jiangping Hu, Haitao Yang,* and Hong-Jun Gao**

With unprecedented energy efficiency and quantum-ready properties, superconducting electronics drive breakthroughs in quantum processors, ultra-precise sensors, and beyond-Moore's-law computing architectures. While nonreciprocal circuit elements such as superconducting diodes are essential for these systems, the realization of practical devices with robust performance remains a major challenge. In particular, polarity-tunable superconducting diodes that operate efficiently under zero magnetic field are highly desired for practical applications. Here, a polarity-reversible zero-field Josephson diode effect (JDE) is demonstrated with highly sustained performance in a vertically stacked 2D van der Waals (vdW) ferromagnetic Josephson junction composed of the Ising superconductor NbSe$_2$ and the itinerant ferromagnet Fe$_3$GeTe$_2$ (FGT) layers. The diode asymmetry and rectification polarity are primarily tunable via the magnetic state and thickness of the FGT layer. By optimizing the thickness of the FGT layer, a polarity-reversible JDE is achieved with a rectification efficiency of up to 34.1%. Furthermore, an exclusive OR (XOR) logic gate operation is successfully implemented using this reconfigurable JDE. The work establishes a new route toward realizing efficient, polarity-reversible, zero-field superconducting diodes and underscores their potential for 2D non-dissipative superconducting electronics.

1. Introduction

The relentless scaling of computational power density, driven by Moore's Law, has precipitated a critical energy bottleneck in modern data centers. Superconducting electronics, particularly when coupled with recent breakthroughs in high-efficiency cryogenic cooling,[1] have emerged as a revolutionary pathway toward ultralow-power computing.[2–4] A foundational component of such architectures is the superconducting diodes, an analog to its semiconductor counterparts, capable of enabling unidirectional flow of supercurrent.[5–7] The key characteristic of these superconducting diodes is the nonreciprocal critical current, whose directionality, termed polarity, is governed by engineered breaking of inversion and/or time-reversal symmetry (TRS), often via artificial structural asymmetries or applied magnetic fields.[8–10] Importantly, the realization of superconducting diodes with a tunable polarity unlocks avenues for novel reconfigurable logic gates and memory cells, and enables dynamically programmable nonreciprocal components such as isolators and rectifiers through polarity modulation,[11] which are essential for the high-frequency low-loss signal processing.[12–15] Achieving the zero-field superconducting diode effect (SDE) with a tunable polarity represents a critical milestone toward practical, non-dissipative electronics.

Despite theoretical promise and experimental advances in SDE,[8,16–25] most demonstrations to date require external magnetic fields to break TRS,[19,21,26–28] limiting their applicability. Some efforts have focused on intrinsic TRS breaking in unconventional superconductors, including the kagome superconductor CsV$_3$Sb$_5$,[29] iron-based superconductor FeSe$_x$Te$_{1-x}$,[30,31] and cuprate Bi$_2$Sr$_2$CaCu$_2$O$_{8+\delta}$.[26,32] However, these systems typically suffer from low diode efficiencies <20% and stochastic or irreproducible polarity control. Alternatively, superconductor-ferromagnet heterostructures exploit interfacial magnetization or magnetic proximity effects to break TRS.[9,11,18,33–36] Such configurations allow the polarity regulation by modulating ferromagnetic moments. Examples include non-centrosymmetric

---

G. Hu, Y. Han, H. Guo, S. Lv, Y. Wang, Z. Zhao, K. Zhu, Q. Qi, G. Xian, S. Zhu, L. Bao, K. Jiang, J. Hu, H. Yang, H.-J. Gao
Beijing National Center for Condensed Matter Physics and Institute of Physics
Chinese Academy of Sciences
Beijing 100190, P. R. China
E-mail: jiangkun@iphy.ac.cn; htyang@iphy.ac.cn; hjgao@iphy.ac.cn

G. Hu, Y. Han, H. Guo, S. Lv, T. Gao, Y. Wang, Z. Zhao, K. Zhu, Q. Qi, S. Zhu, L. Bao, X. Lin, W. Zhou, H. Yang, H.-J. Gao
School of Physical Sciences
University of Chinese Academy of Sciences
Beijing 100049, P. R. China
E-mail: wuzhou@ucas.ac.cn

G. Xian, L. Bao
Songshan Lake Materials Laboratory
Dongguan, Guangdong 523808, P. R. China

The ORCID identification number(s) for the author(s) of this article can be found under https://doi.org/10.1002/adma.202513434

DOI: 10.1002/adma.202513434

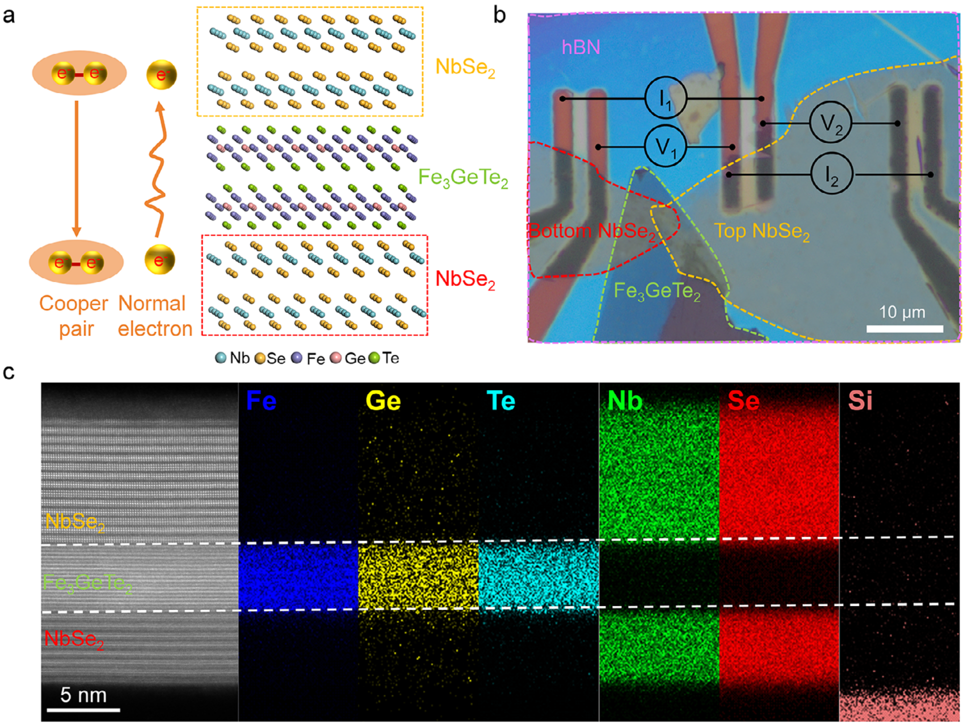

Figure 1. Vertically stacked NbSe$_2$/FGT/NbSe$_2$ Josephson junction(S/F/S junction) with atomically sharp interfaces. a) Schematic illustration of the S/F/S junction, where the junction shows normal electron tunnelling in one direction but superconductivity in the other (Cooper pair tunnelling). b) Optical image of a heterostructure device with a two-channel configuration: the left channel features the S/F/S junction, while the right channel comprises the top NbSe$_2$ layer. The red, green, yellow, and pink dashed lines demarcate the bottom NbSe$_2$, FGT, top NbSe$_2$, and hBN encapsulation layers, respectively. c) Cross-sectional STEM-ADF image and corresponding EDS mappings of Fe (blue), Ge (yellow), Te (cyan), Nb(green), Se(red), and Si (pink). An atomically sharp interface is resolved between NbSe$_2$ and FGT layers.

superconducting/ferromagnetic superlattices[18] and lateral Josephson junctions incorporating $Y_3Fe_5O_{12}$-magnetized Pt barriers.[9] However, interfacial imperfections, such as the lattice mismatch, interdiffusion, and magnetic disorder, remain formidable obstacles and degrade the device performance, necessitating atomic-level interface engineering.

To transcend these limitations, vdW ferromagnetic Josephson junctions offer a transformative architecture. The atomically precise layer-by-layer stacking of vdW heterostructures eliminates defects like dangling bonds inherent to epitaxial systems. In addition, the asymmetry interfaces between superconducting and ferromagnetic layers can break inversion symmetry, and the intrinsic magnetization of the ferromagnetic barrier can induce TRS breaking.[37–39] This dual symmetry breaking, achieved without external fields, precisely meets the essential theoretical criteria for realizing a zero-field SDE. Therefore, vdW ferromagnetic Josephson junctions provide a compelling route toward the highly efficient, polarity-tunable zero-field SDE operating at the 2D limit. Despite these advantages, a definitive experimental demonstration of polarity-tunable zero-field SDE in this system remains elusive.

In this work, we construct high-quality vdW ferromagnetic Josephson junctions, NbSe$_2$/FGT/NbSe$_2$ (S/F/S), comprising the Ising superconducting NbSe$_2$ and the ferromagnetic barrier FGT with a strong perpendicular magnetic anisotropy. These junctions manifest a robust zero-field JDE, as demonstrated by asymmetric current-voltage (V-I) curves in the absence of an external magnetic field. The observed half-wave rectification maintains exceptional stability across over 10^4 repeated pulsed measurements, indicating the high reliability and durability of the zero-field JDE. Critically, both the magnitude and polarity of the zero-field JDE can be flexibly tuned via multiple parameters within the junction, including the magnetic configuration, superconducting state, and thickness of the FGT layer. By optimizing the thickness of the FGT layer, we achieve a large diode efficiency of 34.1% under zero-field conditions. Leveraging the polarity-reversible zero-field JDE, we further demonstrate a XOR logic gate operation, showcasing the potential of these junctions in advancing energy-efficient superconducting logic circuits and hybrid superconducting spintronics.

2. Results and Discussion

2.1. Vertically Stacked NbSe$_2$/FGT/NbSe$_2$ Josephson Junction

The device architecture is illustrated in **Figure** 1a, where a vertically structured Josephson junction was fabricated by encapsulating a thin FGT layer between two superconducting NbSe$_2$ layers. The single crystals of FGT and NbSe$_2$ were synthesized via chemical vapor transport (CVT), and their X-ray diffraction (XRD) patterns exhibit characteristic (00l) diffraction peaks, indicating the c-axis orientation and high crystallinity (Figure S1, Supporting Information). NbSe$_2$, as a type-II s-wave superconductor, can show the Ising superconductivity in NbSe$_2$ few layers or monolayer,

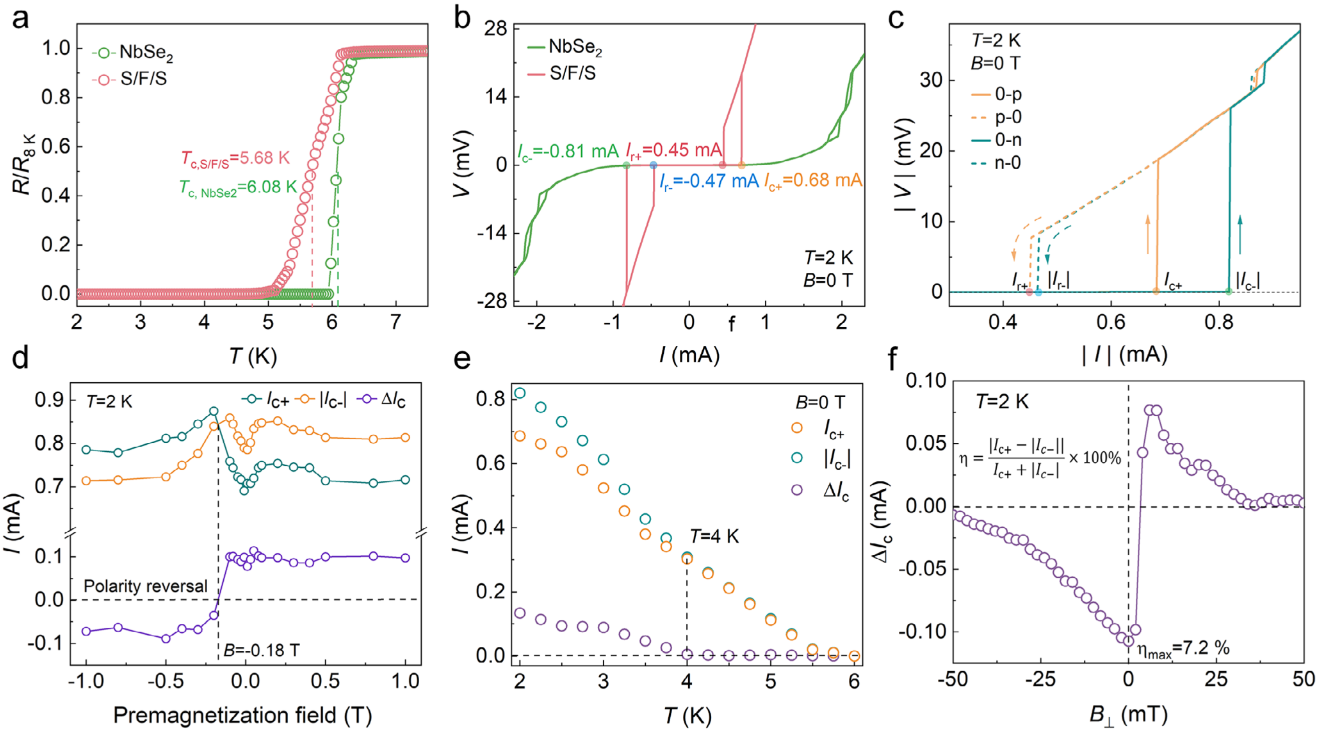

Figure 2. Zero-field Josephson diode effect in the S/F/S junction (Device 1). a) Temperature-dependent resistance of the S/F/S junction and the top $NbSe_2$ layer measured by a four-terminal configuration. b) *V-I* curves of the S/F/S junction and the top $NbSe_2$ layer at 2 K under zero magnetic field. c) *V-I* curves with the positive sweep, where the yellow solid and dashed lines correspond with the 0–p and p–0 branches, respectively, and the green solid and dashed lines correspond with the 0–n and n–0 branches, respectively. The positions of the critical current I_{c+}, $|I_{c-}|$, I_{r+}, and $|I_{r-}|$ are marked. d) Pre-magnetized magnetic field dependence of the critical supercurrent I_c and non-reciprocal component ΔI_c in the S/F/S junction. The non-reciprocal component of the critical current is defined as $\Delta I_c = |I_{c+} - |I_{c-}||$. e) Temperature dependence of I_c and ΔI_c in the S/F/S junction. f) The magnetic field dependence of ΔI_c in the S/F/S junction at 2 K. The superconducting diode efficiency is defined as $\eta = \frac{|I_{c+} - |I_{c-}||}{I_{c+} + |I_{c-}|} \times 100\%$, and the maximum efficiency η_{max} under the magnetic field is 7.2 %.

which originates from the combination of broken inversion symmetry and strong spin-orbit interaction (SOI). While this phenomenon disappears in $NbSe_2$ multilayer or bulk forms (Section S2, Supporting Information).[40–42] FGT is a vdW ferromagnetic metal, and magnetic measurements reveal the Curie temperature of 220 K and strong perpendicular magnetic anisotropy (Section S3, Supporting Information).

The S/F/S heterostructure was fabricated using a modified dry transfer technique in an argon glovebox, encapsulated by the top hexagonal boron nitride (hBN) layer to prevent oxidation and degradation. A parallel six-electrode configuration in Figure 1b was employed to separately measure the properties of the S/F/S junction and a reference few-layer $NbSe_2$ (Device 1). The thickness of the top and bottom $NbSe_2$ layers in Device 1 is ≈10 and 7 nm, respectively, both of which exhibit the Ising superconductivity (Figure S2, Supporting Information). The FGT layer has a thickness of 7 nm, which exhibits the hard magnetic property, and the saturation magnetic field of 0.51 T (Figure S3-2, Supporting Information). Cross-sectional scanning transmission electron microscopy (STEM) measurements in Figure 1c resolve atomically sharp interfaces between the $NbSe_2$ and FGT layers in the S/F/S junction. Moreover, twist angles between the top/bottom $NbSe_2$ and FGT layers, as well as intrinsic defects and strains within the few-layered system, can break inversion symmetry in the junction.

2.2. Zero-Field Josephson Diode Effect in the S/F/S Junction

As depicted in **Figure** 2a, when cooling Device 1 to low temperatures under the zero magnetic field, the resistance of few-layer $NbSe_2$ exhibits a sharp superconducting transition with a superconducting transition temperature ($T_{c,\ NbSe2}$) of 6.08 K. In contrast, the resistance of the S/F/S junction drops to zero, undergoing a broader temperature range, which indicates that the $NbSe_2$ induces a superconducting state in the ferromagnetic FGT layer. The corresponding superconducting transition temperature for this induced state is $T_{c,\ S/F/S} = 5.68$ K. The typical voltage-current- characteristics (*V-I*) curves of the S/F/S junction and few-layer $NbSe_2$ at 2 K under zero magnetic field are shown in Figure 2b. The *V-I* curve of the S/F/S junction exhibits distinct hysteresis loops, which can be attributed to the resistively and capacitively shunted junction model.[30,43] In this model, the capacitance in the junction causes different critical currents when breaking the superconducting state (I_c) and returning to it (I_r). The critical currents of the S/F/S junction show a significant difference. However, the critical current of the few-layer $NbSe_2$ is much larger than that of the S/F/S junction, and no hysteresis or difference between I_{c+} and $|I_{c-}|$ is observed, indicating that the non-reciprocal behavior originates from the S/F/S structure itself rather than external effects.

As shown in Figure 2c, the hysteretic $V-I$ loop can be divided into four branches: from zero to positive (0-p), positive to zero (p-0), zero to negative (0-n), and negative to zero (n-0). In the positive current range, the critical currents are defined as the I_{c+} and I_{r+}, while in the negative range, they are denoted as the I_{c-} and I_{r-}. The absolute value of I_{c-} is significantly larger than that of I_{c+}, with a difference ΔI_c ($\Delta I_c = |I_{c-}|$-I_{c+}) reaching up to 0.13 mA, while the absolute value of I_{r-} is slightly larger than that of I_{r+}, with a $\Delta I_r = |I_{r-}|$-I_{r+} being ≈0.02 mA. This asymmetry in the critical currents demonstrates a clear non-reciprocal behavior in the S/F/S junction, suggesting the breaking of the inversion symmetry. The difference between I_{r+} and I_{r-} further supports this conclusion. Additionally, the *V-I* curves were swept from negative to positive, then from positive to negative (defined as positive sweep), and swept in the reverse direction (defined as negative sweep) (Figure S4-1, Supporting Information). The *V-I* curves for the positive and negative sweep are totally overlapping, further confirming that the asymmetry in critical currents is an intrinsic property of the junction and not induced by the Joule heating.[20,32] In a ferromagnetic Josephson junction, the combined effect of ferromagnetism and spin-orbit coupling (SOC) makes the current–phase relation (CPR) to acquire an additional phase shift φ_0. The presence of φ_0 is the underlying origin of the zero-field JDE.[9,44]

The φ_0 shift in the S/F/S junction originates from the intrinsic magnetization of the FGT layer, therefore, the zero-field JDE can be efficiently modulated via applying a pre-magnetized out-of-plane magnetic field. Figure 2d displays the evolution of I_{c+}, $|I_{c-}|$ and ΔI_c of the S/F/S junction as a function of the different pre-magnetized out-of-plane magnetic fields measured under the zero magnetic field at 2 K. When the applied negative pre-magnetizing field is smaller than the saturation magnetization of the FGT layer, the magnetization of the FGT layer remains aligned, and the diode polarity does not change. In contrast, once the negative pre-magnetizing field exceeds the saturation field of the FGT layer, the magnetization of the FGT layer reverses; consequently, the polarity of JDE is inverted. Within the range of positive pre-magnetizing fields, the I_{c+}, $|I_{c-}|$ and ΔI_c show a monotonical increase in the range from 0 to 0.2 T, followed by a slight decrease between 0.2 T and 0.5 T, and remain nearly unchanged beyond 0.5 T. The monotonic increase in the range from 0 to 0.2 T may originate from the enhanced out-of-plane magnetization of the FGT layer as the pre-magnetizing field increases. Furthermore, the temperature dependence of I_{c+}, $|I_{c-}|$ and ΔI_c are shown in Figure 2e. As the temperature increases, both critical currents decrease due to the suppression of the superconductivity, with the zero-field JDE persisting up to 4 K, below $T_{c,\ S/F/S}$ of 5.68 K.

The *V-I* curves were recorded while sweeping the magnetic field from −50 to +50 mT at 2 K, and the magnetic field dependence of I_{c+} and $|I_{c-}|$ was extracted and plotted in Figure S4-4 (Supporting Information). The critical current I_{c+} and $|I_{c-}|$ exhibit obvious nonreciprocal components under a small range of the magnetic field. As shown in Figure 2f, the variation of ΔI_c with respect to the magnetic field reveals that ΔI_c reaches a negative maximum of ΔI_c under the zero field, and reduces to zero at ≈+3.6 mT, then changes the polarity and appears a positive peak ≈+7.7 mT. The field modulation of asymmetry indicates an apparent field-induced SDE,[10,21,45] while the noticeable difference between the negative and positive field dependencies is a field-free SDE, which is attributed to the intrinsic magnetic order in the S/F/S junction. To quantify the strength of the diode effect, we define the superconducting diode efficiency as $\eta = \frac{|I_{c+}-|I_{c-}||}{I_{c+}+|I_{c-}|} \times 100\%$. The diode efficiency in Device 1 reaches a maximum of 7.2% under the zero field.

2.3. Polarity-Reversible Half-Wave Rectification with a Sustained Performance

The application of a pre-magnetized magnetic field not only modulates the magnitude of the zero-field JDE but also enables the direct reversal of its polarity when the direction of the magnetic field is inverted. As demonstrated in **Figure 3**a, when applying an out-of-plane magnetic field of −0.5 T (beyond the saturated magnetic field of FGT) to pre-magnetize Device 1, the zero-field JDE exhibits a positive polarity ($I_{c+} > |I_{c-}|$). A square-wave excitation current of 0.84 mA exceeding $|I_{c-}|$ (0.87 mA) but below I_{c+} (0.79 mA) is applied, the positive half-cycle remains in the superconducting state while the negative half-cycle exhibits a voltage drop, achieving the rectification (Figure 3b). To assess the durability of the zero-field JDE, the device was subjected to 10 000 continuous cycles under a square-wave excitation current with an amplitude of 0.84 mA at 1 Hz under zero field (Figure 3c). The Half-wave rectification behavior remains stable throughout the entire cycle count, demonstrating the high reliability and durability of the zero-field JDE. Conversely, with the pre-magnetization under a magnetic field of 0.5 T, the zero-field JDE exhibits a negative polarity ($|I_{c-}| > I_{c+}$) (Figure 3d). When applying a square-wave excitation current of 0.82 mA to Device 1, the rectification characteristic was reversed (Figure 3e). As demonstrated in Figure 3f, the negative half -wave rectification behavior during 10 000 continuous cycles also exhibits a highly durable performance. The sustained rectification over an extended period further indicates that the Joule heating does not significantly affect the device performance, reinforcing the conclusion that the non-reciprocal critical currents are intrinsic to the S/F/S junction rather than an artifact of thermal effects.

2.4. FGT Thickness-Tunable Zero-Field JDE in the S/F/S Junction

Considering the thickness-dependent saturation magnetic moment and coercivity of the FGT layer,[46] we systematically engineered S/F/S junctions with controlled FGT thickness variations while maintaining the constant thickness of the $NbSe_2$ layer to modulate the zero-field JDE. As shown in Figure S7-1,2 (Supporting Information), all the fabricated devices exhibit distinct nonreciprocal features in their *V-I* characteristics. The critical current I_c and its non-reciprocal component ΔI_c of these junctions basically show a decreasing trend as the thickness of the FGT layer increases, whereas the diode efficiency exhibits a pronounced non-monotonic dependence on the thickness of the FGT layer, reaching a maximum for the thickness in the range of 28–34 nm (Figure S7-3, Supporting Information). In particular, the device

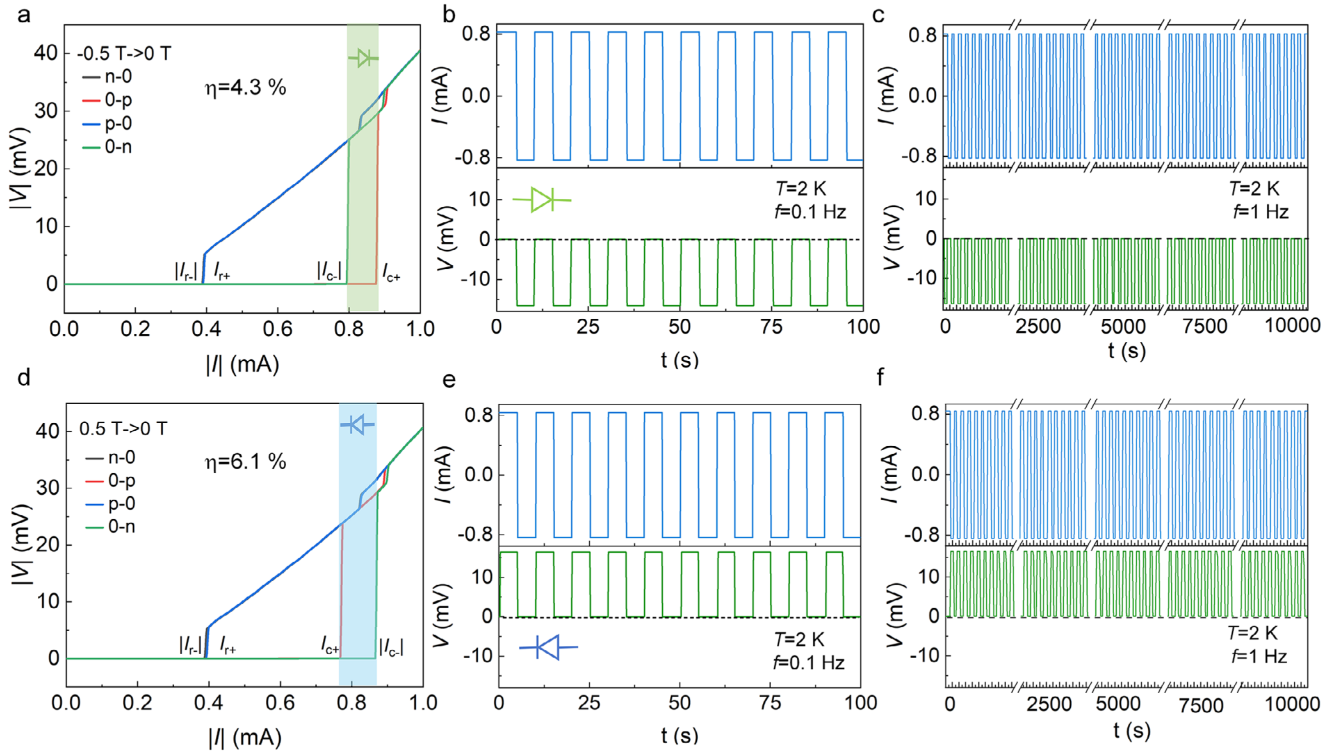

Figure 3. Polarity-reversible half-wave rectification in the S/F/S junction (Device 1) with a highly durable performance. a) *V-I* curves of the S/F/S junction at 2 K under the zero magnetic field after applying a pre-magnetized magnetic field of -0.5 T. The zero-field JDEs exhibit a positive polarity ($I_{c+} > |I_{c-}|$). b) Half-wave rectification of the zero-field JDE in the S/F/S junction at 2 K after applying a pre-magnetized magnetic field of -0.5 T. The top panel shows the applied square-wave excitation with an amplitude of 0.84 mA and a frequency of 0.1 Hz. The bottom panel displays the corresponding measured junction voltage, which is zero during the positive current bias and finite during the negative current bias. The black dotted line indicates the zero-voltage level. c) Durability test of the zero-field diode effect at 2 K. The top panel is the applied square-wave excitation with an amplitude of 0.84 mA and frequency of 1 Hz over 10000 cycles. The bottom panel is the corresponding measured junction voltage during the cycling. d) *V-I* curves of the S/F/S junction at 2 K under the zero magnetic field after applying a pre-magnetized magnetic field of 0.5 T. The zero-field JDEs exhibit the negative polarity ($|I_{c-}| > I_{c+}$). e) Half-wave rectification of the zero-field JDE in the S/F/S junction at 2 K after applying a pre-magnetized magnetic field of 0.5 T. The top panel shows the applied square-wave excitation with an amplitude of 0.82 mA and a frequency of 0.1 Hz. The bottom panel displays the corresponding measured junction voltage, which is zero during the negative current bias and finite during the positive current bias. The black dotted line indicates the zero-voltage level. f) The top panel is the applied square-wave excitation with an amplitude of 0.82 mA and frequency of 1 Hz over 10 000 cycles. The bottom panel is the corresponding measured junction voltage during the cycling.

with a 32-nm-thick FGT layer (Device 2) reaches an exceptionally high diode efficiency of 34.1 %. To elucidate the microscopic origin of this anomalous behavior, we fit the data with an exponential decay function $\exp(-d/\xi)$ and obtained an estimated coherence length $\xi = 31 \pm 8$ nm[47,48] (Figure S11-1, Supporting Information). However, by using the relation $\xi_s \approx \sqrt{\frac{\hbar D}{E_{ex}}}$,[49,50] where D and E_{ex} are the FGT electron diffusion coefficient and exchange field, respectively, we obtain the coherence length of the spin-singlet supercurrent in the FGT layer to be ≈3.5 nm. This value is far smaller than the thickness of the FGT layer in Device 2, indicating that the supercurrent in Device 2 possesses a spin-triplet character. The spin-polarized triplet component may enhance the additional phase shift φ_0, thereby generating the large diode efficiency.

Moreover, T_c of these devices exhibits a pronounced nonmonotonic dependence on the thickness of the FGT layer (Figure S11-2, Supporting Information). An increase of T_c is indicative of a transition from the 0-phase to π-phase. Notably, the variation of T_c is consistent with the trend of the diode efficiency, indicating that the enhancement of the diode efficiency in the devices with the thick FGT layers may be related with the π-phase transition. Consequently, we propose that the exceptionally high diode efficiency observed in Device 2 is related to the spin-polarized triplet superconductivity and π-phase transition (see Section S11, Supporting Information for a detailed discussion).

We performed a detailed study focusing on Device 2, where the thickness of the FGT layer far exceeds the out-of-plane coherence length of $NbSe_2$. As illustrated in **Figure** 4a, the resistance of this device exhibits a pronounced zero-resistance state below the superconducting transition temperature of 5 K. The FGT with a thickness of ≈32 nm in Device 2 exhibits a fragmented magnetic domain structure, which is directly imaged at 4 K using a magnetic force microscope (MFM) without applying an external magnetic field (inset of Figure 4a). Such a magnetic domain structure introduces the interfacial magnetic inhomogeneity in the s-wave superconductor/ferromagnetic junction. This inhomogeneity can facilitate the spin mixing and spin rotation processes of spin-singlet Cooper pairs at the superconducting interfaces, leading to the generation of spin-polarized spin-triplet Cooper pairs.[22,51–53]

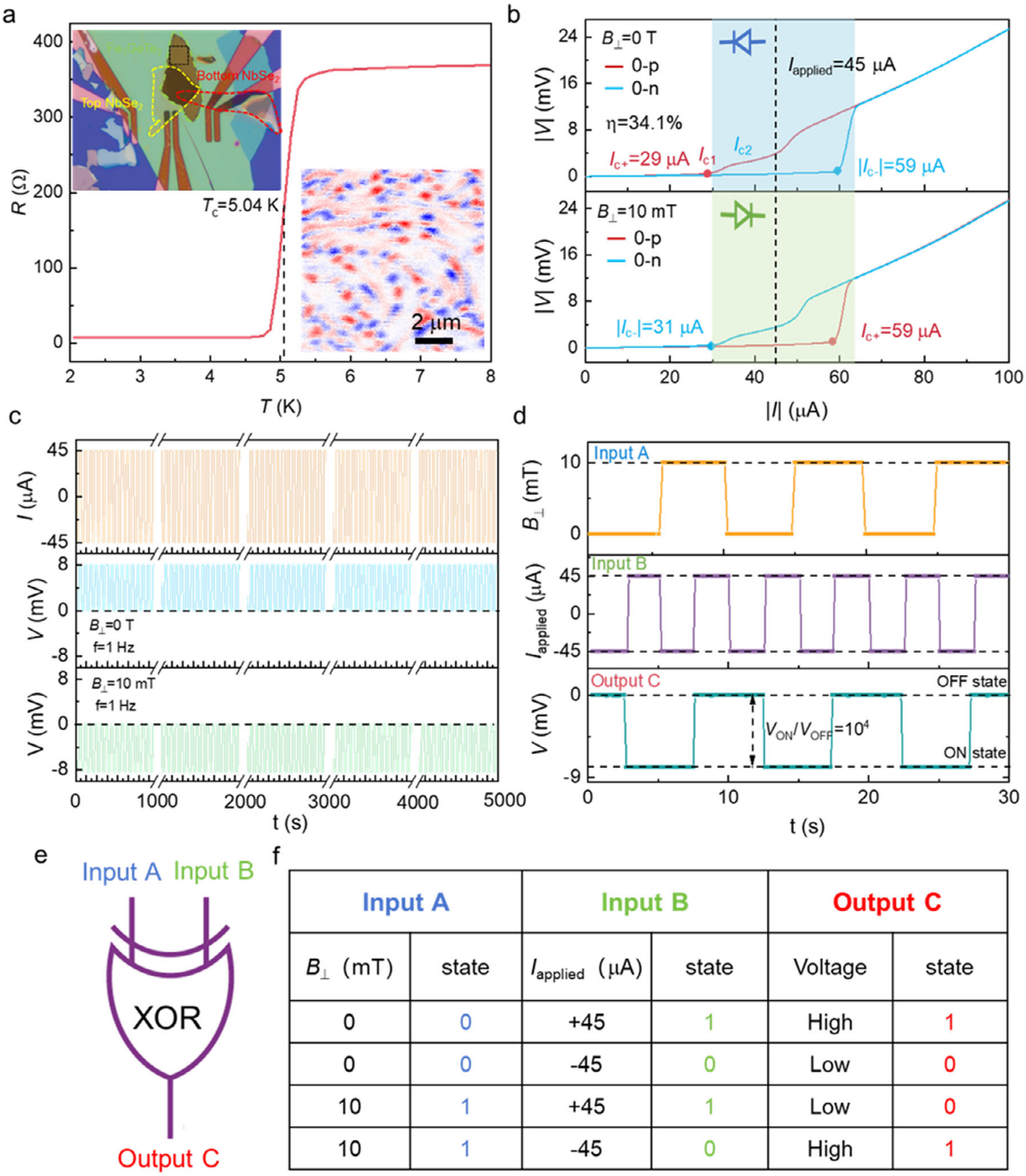

Input A		Input B		Output C	
$B_\perp$ (mT)	state	$I_{applied}$ (μA)	state	Voltage	state
0	0	+45	1	High	1
0	0	-45	0	Low	0
10	1	+45	1	Low	0
10	1	-45	0	High	1

Figure 4. The polarity-reversible zero-field JDE in Device 2 and the XOR logic gate operation. a) Temperature-dependent resistance of Device 2. The left inset provides the optical micrograph of Device 2 with the region marked by the dashed black box, for the magnetic domain structure measured by MFM. The right inset shows the magnetic domain structure of the FGT layer under a zero magnetic field, imaged by the MFM. b) *V-I* curves of Device 2 at 2 K under different magnetic fields. The critical current from 0-p branch is defined as $I_{c+,}$ and the critical current from 0-n branch is denoted as I_{c-}. c) Durability test of JDE in Device 2 at 2 K under different magnetic fields. The top panel illustrates the applied square-wave excitation with an amplitude of 45 μA and a frequency of 1 Hz over 5000 cycles. The bottom panel shows the corresponding measured junction voltage during cycling, demonstrating the stable operation. The black dashed lines indicate the zero-voltage levels. d) Deterministic switching of the polarity state by applying a pulsed magnetic field of 10 mT and pulsed current in Device 2, and the corresponding rectification behaviors. e) The schematic diagram of the XOR logic gate. The "Input B" under different signals of "Input A" can generate a distinct electrical "Output C". f) The truth table with the applied pulsed magnetic field and pulsed current as input signals and the XOR gate operation.

The V-I characteristics of Device 2 in Figure 4b exhibit no pronounced hysteresis, indicating that the junction operates in an overdamped regime with a low resistance-capacitance product. However, there is a significant asymmetry between I_{c+} and $|I_{c-}|$, reflecting a prominent zero-field JDE. Furthermore, we observed that the V-I characteristics of Device 2 show two distinct superconducting critical currents, which can be defined as I_{c1} and I_{c2}. This phenomenon is likely attributed to the tunneling of Cooper pairs within different magnetic domain structures (detailed analysis in Section S12, Supporting Information).[54] Notably, JDE under the magnetic field of 10 mT exhibits the opposite polarity but almost an equal diode efficiency compared to that under the zero field. As shown in Figure S13-3 (Supporting Information), the second-harmonic signals indicate that this magnetic-field-induced polarity reversal primarily originates from a non-reciprocal CPR in the Josephson junction (see Section S13, Supporting Information, for a detailed discussion). Furthermore, we performed the durability of JDE in Device 2. As shown in Figure 4c, when a square-wave excitation current of 45 μA was applied to the device under the zero field and 10 mT, a polarity-reversible and persistent rectification behavior is demonstrated. These results highlight the high efficiency and stability of the polarity-reversible JDE in Device 2 under practical operating conditions.

2.5. XOR Logic Gate Enabled by the Polarity-Reversible JDE

Taking advantage of the polarity-reversible JDE in Device 2, we demonstrate a XOR logic gate operation. As depicted in Figure 4d, a pulsed magnetic field can switch the JDE polarity state in Device 2. Under the zero field, an applied current I_{applied} of −45 μA corresponds to the superconducting state (voltage $< 2 \times 10^{-4}$ mV), defined as the OFF state, while +45 μA results in a finite voltage state (≈7.8 mV), defined as the ON state. Conversely, applying a 10 mT magnetic field reverses these ON and OFF states for the same current magnitudes. Notably, the polarity-reversible JDE achieves an outstanding on/off voltage contrast exceeding four orders of magnitude.[11]

Consequently, the pulsed magnetic field serves as the control input (Input A), determining the nonreciprocal transport polarity: 0 mT ($\Delta I_c<0$, logic "0") and 10 mT ($\Delta I_c>0$, logic "1"). The input current pulses (Input B) provide the data input: a positive pulse (+45 μA) represents logic "1" and a negative pulse (−45 μA) represents logic "0". By cross-modulating these two inputs through the polarity-reversible diode behavior, we achieve a distinguishable electrical output (Output C) that implements the XOR functionality (Figure 4e). As shown in Figure 4f, when the polarity state and input state are set to (0,1) and (1,0), the output logic state is "1" (high voltage). In contrast, when the inputs are (0,0) or (1,1), the output state is "0" (low voltage). These results confirm the successful realization of an XOR gate based on the polarity-reversible JDE, highlighting its potential for low-power-consumption integrated circuit applications.

3. Conclusion

In summary, we have demonstrated a polarity-reversible zero-field JDE with highly durable half-wave rectification behavior in vertically stacked vdW $NbSe_2$/FGT/$NbSe_2$ ferromagnetic Josephson junctions. The underlying JDE originates from the non-reciprocal CPR caused by the combined effect between strong SOI at the asymmetric $NbSe_2$/FGT interface and the spontaneous magnetization of the ferromagnetic layer. Therefore, the magnitude and polarity of this zero-field JDE can be systematically modulated via pre-magnetized magnetic fields, temperatures variations, and the thickness of the FGT layer. Notably, by tuning the thickness of the ferromagnetic layer, we achieved a maximum superconducting diode efficiency of 34.1%. Based on the high-efficiency and polarity-reversible JDE, we further implement a XOR logic gate operation. These findings establish a fundamental connection between the superconducting phase coherence and ferromagnetic state in hybrid ferromagnetic-superconducting systems, while simultaneously pioneering a pathway toward non-dissipative superconducting logic circuits and hybrid spintronic devices enabled by vdW heterostructures.

4. Experimental Section

Single Crystal Growth: High-quality single crystals of FGT and $NbSe_2$ were synthesized using a CVT method. Stoichiometric amounts of high-purity elemental components and iodine were mixed and sealed in quartz tubes. These tubes were then placed in a two-zone tubular furnace, where the source and growth zones were heated to their respective target temperatures and maintained for two weeks. Shiny single crystals were obtained after cooling the system to room temperature. Detailed procedures can be found in the previous work.[55]

Characterization Techniques: The crystal structures of FGT and $NbSe_2$ were analyzed using XRD. The magnetic properties of the crystals were measured with a vibrating sample magnetometer (VSM, Quantum Design PPMS-16 T). The thicknesses of the FGT and $NbSe_2$ layers were determined using a Cypher S atomic force microscope (Oxford Instruments, Asylum Research, Santa Barbara, USA). Samples for STEM characterization were prepared via focused ion beam (FIB) milling and were performed on an aberration-corrected JEOL GRANDARM2 microscope operated at 200 kV. The beam convergence semi-angle was set to 32 mrad, while the collection semi-angles were 68–280 mrad for high-angle annular dark-field (HAADF) images and 17 mrad for annular bright-field (ABF) images.

Device Fabrication: The bottom electrodes were patterned on a SiO_2/Si substrate using ultraviolet lithography, followed by the thermal evaporation of Cr/Au (3/17 nm). Mechanical exfoliation and dry transfer processes were conducted in a glove box with controlled oxygen and moisture levels (O_2, H_2O < 0.1 ppm). Polydimethylsiloxane (PDMS) stamps were soaked in an isopropanol solution for one week and then air-dried to minimize the residual adhesion. The desired $NbSe_2$ layer was transferred onto the parallel electrodes using PDMS, ensuring that the bottom $NbSe_2$ layer spanned two electrodes. Subsequently, an FGT layer was stacked on top of the bottom $NbSe_2$ layer. The top $NbSe_2$ layer was then placed on the FGT layer to form an overlapping region with the bottom $NbSe_2$ layer, and avoiding direct contact between them. Finally, a hBN layer was used to encapsulate the heterostructure for protection.

Electrical Transport Measurements: Electrical transport measurements were conducted in a Quantum Design Physical Property Measurement System (PPMS) using a Keithley 6221 current source and a Keithley 2182A nanovoltmeter. The resistance versus temperature (R-T) curves, voltage-current characteristics (V-I), differential conductance (dV/dI), and half-wave rectification were measured in a four-probe configuration.

Data Processing: The critical current is defined as the DC current bias at the onset of voltage in the V-I curves, where the I_{c+} and I_{c-} represent the critical currents in the positive and negative current directions, respectively. The superconducting transition temperature (T_c) is defined as the temperature at where the resistance reaches half of the normal resistance.

Supporting Information

Supporting Information is available from the Wiley Online Library or from the author.

Acknowledgements

The work is supported by grants from the National Key Research and Development Projects of China (2022YFA1204100), the National Natural Science Foundation of China (62488201, 1240041502), the CAS Superconducting Research Project (SCZX-0101), the Innovation Program of Quantum Science and Technology (2021ZD0302700), the CAS Project for Young Scientists in Basic Research (YSBR-053). This research benefited from resources and support from the Electron Microscopy Center at the University of Chinese Academy of Sciences.

Conflict of Interest

The authors declare no conflict of interest.

Author Contributions

G.H. and Y.H. contributed equally to this work. H.T.Y. and H.J.G. designed the project. K.J. and J.P.H. provided the theoretical guidance. G.J.H. and Y.C.H. prepared the samples, performed the electrical transport measurements, and work with the data. T.Q.G and W.Z. performed the STEM measurements. S.H.L. performed the VSM measurements. Y.H.W and S.Y.Z performed the MFM measurements. Z.Z. and X.L. performed the AFM measurements. H.G. and K.Z. performed the XRD measurement. L.H.B. and Q.Q. performed the processing of micro/nano metal electrodes. All authors participated in the data analysis and manuscript writing.

Data Availability Statement

The data that support the findings of this study are available from the corresponding author upon reasonable request.

Keywords

Ising superconductor $NbSe_2$, itinerant ferromagnet Fe_3GeTe_2, van der waals ferromagnetic Josephson junction, XOR logic operation, zero-field Josephson diode effect

Received: July 16, 2025
Revised: November 2, 2025

---

[1] R. Radebaugh, *J. Phys.: Condens. Matter* **2009**, *21*, 164219.
[2] A. I. Braginski, *J. Supercond. Novel Magn.* **2018**, *32*, 23.
[3] A. Silver, A. Kleinsasser, G. Kerber, Q. Herr, M. Dorojevets, P. Bunyk, L. Abelson, *Supercond. Sci. Technol.* **2003**, *16*, 1368.
[4] T. V. Duzer, *Cryogenics* **1990**, *30*, 980.
[5] K. Jiang, J. Hu, *Nat. Phys.* **2022**, *18*, 1145.
[6] Y. Zhang, Y. Gu, P. Li, J. Hu, K. Jiang, *Phys. Rev. X* **2022**, *12*, 041013;
[7] J. Ma, R. Zhan, X. Lin, *Adv. Phys. Res.* **2025**, *4*, 2400180.
[8] F. Ando, Y. Miyasaka, T. Li, J. Ishizuka, T. Arakawa, Y. Shiota, T. Moriyama, Y. Yanase, T. Ono, *Nature* **2020**, *584*, 373.
[9] K.-R. Jeon, J.-K. Kim, J. Yoon, J.-C. Jeon, H. Han, A. Cottet, T. Kontos, S. S. P. Parkin, *Nat. Mater.* **2022**, *21*, 1008.
[10] L. Bauriedl, C. Bäuml, L. Fuchs, C. Baumgartner, N. Paulik, J. M. Bauer, K.-Q. Lin, J. M. Lupton, T. Taniguchi, K. Watanabe, C. Strunk, N. Paradiso, *Nat. Commun.* **2022**, *13*, 4266.
[11] J. Xiong, J. Xie, B. Cheng, Y. Dai, X. Cui, L. Wang, Z. Liu, J. Zhou, N. Wang, X. Xu, X. Chen, S. W. Cheong, S. J. Liang, F. Miao, *Nat. Commun.* **2024**, *15*, 4953.
[12] S. Chahid, S. Teknowijoyo, I. Mowgood, A. Gulian, *Phys. Rev. B* **2023**, *107*, 054506.
[13] J. Ingla-Aynés, Y. Hou, S. Wang, E.-D. Chu, O. A. Mukhanov, P. Wei, J. S. Moodera, *Nat. Electron.* **2025**, *8*, 411.
[14] M. Castellani, O. Medeiros, A. Buzzi, R. A. Foster, M. Colangelo, K. K. Berggren, *Nat. Electron.* **2025**, *8*, 417.
[15] D. Kochan, C. Strunk, *Nat. Electron.* **2025**, *8*, 380.
[16] A. Daido, Y. Ikeda, Y. Yanase, *Phys. Rev. Lett.* **2022**, *128*, 037001.
[17] M. Davydova, S. Prembabu, L. Fu, *Sci. Adv.* **2022**, *8*, abo0309.
[18] H. Narita, J. Ishizuka, R. Kawarazaki, D. Kan, Y. Shiota, T. Moriyama, Y. Shimakawa, A. V. Ognev, A. S. Samardak, Y. Yanase, T. Ono, *Nat. Nanotechnol.* **2022**, *17*, 823.
[19] B. Pal, A. Chakraborty, P. K. Sivakumar, M. Davydova, A. K. Gopi, A. K. Pandeya, J. A. Krieger, Y. Zhang, M. Date, S. Ju, N. Yuan, N. B. M. Schröter, L. Fu, S. S. P. Parkin, *Nat. Phys.* **2022**, *18*, 1228.
[20] H. Wu, Y. Wang, Y. Xu, P. K. Sivakumar, C. Pasco, U. Filippozzi, S. S. P. Parkin, Y.-J. Zeng, T. McQueen, M. N. Ali, *Nature* **2022**, *604*, 653.
[21] Y. Hou, F. Nichele, H. Chi, A. Lodesani, Y. Wu, M. F. Ritter, D. Z. Haxell, M. Davydova, S. Ilić, O. Glezakou-Elbert, A. Varambally, F. S. Bergeret, A. Kamra, L. Fu, P. A. Lee, J. S. Moodera, *Phys. Rev. Lett.* **2023**, *131*, 027001.
[22] M. Nadeem, M. S. Fuhrer, X. Wang, *Nat. Rev. Phys.* **2023**, *5*, 558.
[23] J. Hu, C. Wu, X. Dai, *Phys. Rev. Lett.* **2007**, *99*, 067004.
[24] H. F. Legg, D. Loss, J. Klinovaja, *Phys. Rev. B* **2022**, *106*, 104501.
[25] S. Matsuo, T. Imoto, T. Yokoyama, Y. Sato, T. Lindemann, S. Gronin, G. C. Gardner, M. J. Manfra, S. Tarucha, *Nat. Phys.* **2023**, *19*, 1636.
[26] S. Ghosh, V. Patil, A. Basu, A. D. Kuldeep, D. A. Jangade, R. Kulkarni, A. Thamizhavel, J. F. Steiner, F. von Oppen, M. M. Deshmukh, *Nat. Mater.* **2024**, *23*, 612.
[27] P. Chen, G. Wang, B. Ye, J. Wang, L. Zhou, Z. Tang, L. Wang, J. Wang, W. Zhang, J. Mei, W. Chen, H. He, *Adv. Funct. Mater.* **2023**, *34*, 2311229.
[28] M. Gupta, G. V. Graziano, M. Pendharkar, J. T. Dong, C. P. Dempsey, C. Palmstrøm, V. S. Pribiag, *Nat. Commun.* **2023**, *14*, 3078.
[29] T. Le, Z. Pan, Z. Xu, J. Liu, J. Wang, Z. Lou, X. Yang, Z. Wang, Y. Yao, C. Wu, X. Lin, *Nature* **2024**, *630*, 64.
[30] S. Li, Y. Deng, D. Hu, C. Zhu, Z. Yang, W. Tian, X. Wang, M. Yue, Q. Wu, Z. Liu, X. R. Wang, *ACS Nano* **2024**, *18*, 31076.
[31] G. Qiu, H. Y. Yang, L. Hu, H. Zhang, C. Y. Chen, Y. Lyu, C. Eckberg, P. Deng, S. Krylyuk, A. V. Davydov, R. Zhang, K. L. Wang, *Nat. Commun.* **2023**, *14*, 6691.
[32] S. Qi, J. Ge, C. Ji, Y. Ai, G. Ma, Z. Wang, Z. Cui, Y. Liu, Z. Wang, J. Wang, *Nat. Commun.* **2025**, *16*, 531.
[33] E. Strambini, M. Spies, N. Ligato, S. Ilić, M. Rouco, C. González-Orellana, M. Ilyn, C. Rogero, F. S. Bergeret, J. S. Moodera, P. Virtanen, T. T. Heikkilä, F. Giazotto, *Nat. Commun.* **2022**, *13*, 2431.
[34] A. Gutfreund, H. Matsuki, V. Plastovets, A. Noah, L. Gorzawski, N. Fridman, G. Yang, A. Buzdin, O. Millo, J. W. A. Robinson, Y. Anahory, *Nat. Commun.* **2023**, *14*, 1630.
[35] J. Yun, S. Son, J. Shin, G. Park, K. Zhang, Y. J. Shin, J.-G. Park, D. Kim, *Phys. Rev. Res.* **2023**, *5*, L022064.
[36] M. Trahms, L. Melischek, J. F. Steiner, B. Mahendru, I. Tamir, N. Bogdanoff, O. Peters, G. Reecht, C. B. Winkelmann, F. von Oppen, K. J. Franke, *Nature* **2023**, *615*, 628.
[37] L. Ai, E. Zhang, J. Yang, X. Xie, Y. Yang, Z. Jia, Y. Zhang, S. Liu, Z. Li, P. Leng, X. Cao, X. Sun, T. Zhang, X. Kou, Z. Han, F. Xiu, S. Dong, *Nat. Commun.* **2021**, *12*, 6580.

[38] H. Idzuchi, F. Pientka, K. F. Huang, K. Harada, O. Gul, Y. J. Shin, L. T. Nguyen, N. H. Jo, D. Shindo, R. J. Cava, P. C. Canfield, P. Kim, *Nat. Commun.* **2021**, *12*, 5332.
[39] K. Kang, H. Berger, K. Watanabe, T. Taniguchi, L. Forro, J. Shan, K. F. Mak, *Nano Lett.* **2022**, *22*, 5510.
[40] X. Xi, Z. Wang, W. Zhao, J.-H. Park, K. T. Law, H. Berger, L. Forró, J. Shan, K. F. Mak, *Nat. Phys.* **2015**, *12*, 139.
[41] Y. Xing, K. Zhao, P. Shan, F. Zheng, Y. Zhang, H. Fu, Y. Liu, M. Tian, C. Xi, H. Liu, J. Feng, X. Lin, S. Ji, X. Chen, Q.-K. Xue, J. Wang, *Nano Lett.* **2017**, *17*, 6802.
[42] S. C. de la Barrera, M. R. Sinko, D. P. Gopalan, N. Sivadas, K. L. Seyler, K. Watanabe, T. Taniguchi, A. W. Tsen, X. Xu, D. Xiao, B. M. Hunt, *Nat. Commun.* **2018**, *9*, 1427.
[43] K. Misaki, N. Nagaosa, *Phys. Rev. B* **2021**, *103*, 245302.
[44] A. Costa, C. Baumgartner, S. Reinhardt, J. Berger, S. Gronin, G. C. Gardner, T. Lindemann, M. J. Manfra, J. Fabian, D. Kochan, N. Paradiso, C. Strunk, *Nat. Nanotechnol.* **2023**, *18*, 1266.
[45] J.-K. Kim, K.-R. Jeon, P. K. Sivakumar, J. Jeon, C. Koerner, G. Woltersdorf, S. S. P. Parkin, *Nat. Commun.* **2024**, *15*, 1120.
[46] C. Tan, J. Lee, S. G. Jung, T. Park, S. Albarakati, J. Partridge, M. R. Field, D. G. McCulloch, L. Wang, C. Lee, *Nat. Commun.* **2018**, *9*, 1554.
[47] K. R. Jeon, B. K. Hazra, K. Cho, A. Chakraborty, J. C. Jeon, H. Han, H. L. Meyerheim, T. Kontos, S. S. P. Parkin, *Nat. Mater.* **2021**, *20*, 1358.
[48] G. Hu, C. Wang, S. Wang, Y. Zhang, Y. Feng, Z. Wang, Q. Niu, Z. Zhang, B. Xiang, *Nat. Commun.* **2023**, *14*, 1779.
[49] A. I. Buzdin, *Rev. Mod. Phys.* **2025**, *77*, 935.
[50] A. Buzdin, *Phys. Rev. Lett.* **2008**, *101*, 107005.
[51] D. Rana, R. Aswini, G. Basavaraja, C. Patra, S. Howlader, R. Roy Chowdhury, M. Kabir, R. P. Singh, G. Sheet, *Phys. Rev. B* **2022**, *106*, 085120.
[52] R. S. Keizer, S. T. B. Goennenwein, T. M. Klapwijk, G. Miao, G. Xiao, A. Gupta, *Nature* **2006**, *439*, 825.
[53] T. S. Khaire, M. A. Khasawneh, W. P. Pratt, N. O. Birge, *Phys. Rev. Lett.* **2010**, *104*, 137002.
[54] J. Huang, Z. Li, X. Bi, M. Tang, C. Qiu, F. Qin, H. Yuan, *Adv. Mater.* **2024**, *36*, 2314190.
[55] G. Hu, Y. Han, W. Yu, S. Lv, Y. Li, Z. Gong, H. Guo, K. Zhu, Z. Zhao, Q. Qi, G. Xian, L. Bao, X. Lin, J. Pan, S. Du, H. Yang, H.-J. Gao, *Nano Res.* **2025**, *18*, 94907068.